High Resolution Observations of the Near-Surface Wind Field over an Isolated Mountain and in a Steep River Canyon

B.W. Butler[1,4], N.S. Wagenbrenner[1,2], J.M. Forthofer[1], B.K. Lamb[2], K.S. Shannon[1], D. Finn[3], R. M. Eckman[3], K. Clawson[3], L. Bradshaw[1], P. Sopko[1], S. Beard[3], D. Jimenez[1], C. Wold[1], M., Vosburgh[1]

[1]US Forest Service, Rocky Mountain Research Station, Missoula Fire Sciences Laboratory, 5775 Hwy 10 Missoula, MT 59808

[2]Washington State University, Laboratory for Atmospheric Research

Pullman, WA 99164-2910

[3]NOAA Air Resources Laboratory, Field Research Division 1750 Foote Dr.

Idaho Falls, ID 83402

[4]Corresponding Author t:406-329-4801, c:406-239-3665, f:406-329-4825, e:bwbutler@fs.fed.us

Abstract

A number of numerical wind flow models have been developed for simulating wind flow at relatively fine spatial resolutions (e.g., ~100 m); however, there are very limited observational data available for evaluating these high resolution models. This study presents high-resolution surface wind datasets collected from an isolated mountain and a steep river canyon. The wind data are presented in terms of four flow regimes: upslope, afternoon, downslope, and a synoptically-driven regime. There were notable differences in the data collected from the two terrain types. For example, wind speeds on the isolated mountain increased with distance upslope during upslope flow, but generally decreased with distance upslope at the river canyon site during upslope flow. In a downslope flow, wind speed did not have a consistent trend with position on the isolated mountain, but generally increased with distance upslope at the river canyon site. The highest measured speeds occurred during the passage of frontal systems on the isolated mountain. Mountaintop winds were often twice as high as wind speeds measured on the surrounding plain. The highest speeds measured in the river canyon occurred during late morning hours and were from easterly downcanyon flows, presumably associated with surface pressure gradients induced by formation of a regional thermal trough to the west and high pressure to the east. Under periods of weak synoptic forcing, surface winds tended to be decoupled from large-scale flows, and under periods of strong synoptic forcing, variability in surface winds was sufficiently large due to terrain-induced mechanical effects (speed-up over ridges and decreased speeds on leeward sides of terrain obstacles) that a large-scale mean flow would not be representative of surface winds at most locations on or within the terrain feature. These findings suggest that traditional operational weather model (i.e., with numerical grid resolutions of around 4 km or larger) wind predictions are not likely to be good predictors of local near-surface

43 winds at sub-grid scales in complex terrain. Measurement data can be found at:
44 http://www.firemodels.org/index.php/windninja-introduction/windninja-publications.

45

1   Introduction

47 Predictions of terrain-driven winds are important in regions with complex topography
48 for a number of issues, including wildland fire behavior and spread (Sharples et al.,
49 2012; Simpson et al., 2013), transport and dispersion of pollutants (Jiménez et al.,
50 2006; Grell et al., 2000), simulation of convection-driven processes (Banta, 1984;
51 Langhans et al., 2013), wind resource assessment for applications such as wind tur-
52 bine siting (Chrust et al., 2013; Palma et al., 2008), wind forecasting (Forthofer et al,
53 in press), and climate change impacts (Daly et al., 2010). Numerous efforts have
54 focused on improving boundary-layer flow predictions from numerical weather predic-
55 tion (NWP) models by either reducing the horizontal grid size in order to resolve the
56 effects of finer-scale topographical features on atmospheric flow (Lundquist et al.,
57 2010; Zhong and Fast, 2003) or adding new parameterizations to account for unre-
58 solved terrain features (Jiménez and Dudhia, 2012). Because NWP simulations are
59 computationally demanding and suffer from inherent limitations of terrain-following
60 coordinate systems in steep terrain (Lundquist et al., 2010), a number of high resolu-
61 tion diagnostic wind models have also been developed to downscale wind predictions
62 from NWP models in order to meet the needs of the aforementioned applications
63 (e.g., Beaucage et al., 2012). However, there are limited observational data availa-
64 ble to evaluate and improve such high resolution models. This paper describes a
65 research program in which wind data were collected at very high spatial resolution
66 under a range of meteorological conditions for two different types of complex terrain
67 features. The datasets collected enhance the archive of observational data available
68 to evaluate high resolution models. All of the data from the field program are availa-
69 ble   at: http://www.firemodels.org/index.php/windninja-introduction/windninja-
70 publications.

71   Fine-scale (i.e., ~1-100 m) variations in topography and vegetation substantially
72 alter the near-surface flow field through mechanical effects, such as flow separation
73 around obstacles, enhanced turbulence from increased surface roughness and
74 speed-up over ridges, and through thermally-driven flows induced by local differential
75 surface heating in steep terrain (Defant, 1949, Banta, 1984; Banta and Cotton, 1982;
76 Whiteman, 2000, Zardi and Whiteman, 2013, Chrust, et al., 2013). These local scale
77 flow effects are critical for surface wind-sensitive processes, such as wildland fire
78 behavior, where the near-surface wind is often the driving meteorological variable for
79 fire rate of spread and intensity (Rothermel, 1972; Sharples et al., 2012). In order to
80 capture these terrain-induced effects, wind modeling in complex terrain requires that
81 surface characteristics, including terrain, vegetation, and their interactions with the
82 atmosphere, be resolved at a high spatial resolution.

83   Although diagnostic wind models do not typically employ sophisticated boundary
84 layer schemes in their flow solutions, they often incorporate parameterized algo-
85 rithms for specific boundary layer effects, such as thermally-driven winds (e.g., diur-
86 nal slope flows) and non-neutral atmospheric stability (Forthofer et al., 2009; Scire et
87 al., 2000). Evaluation of such schemes has been limited by the types of terrain fea-
88 tures and range of meteorological conditions represented in available observational
89 datasets. For example, the evaluations performed by Forthofer et al. (In Review)

were limited by available surface wind data in complex terrain. The two most widely used datasets for evaluation of high resolution wind predictions were collected on topographically-simple, low elevation hills investigated for wind energy applications such as the site for the Askervein Hill study (Berg et al., 2011; Taylor and Teunissen, 1987). Wind energy research has focused on relatively simple terrain because winds in complicated terrain are more difficult to reliably forecast and have higher turbulence that reduces the life of the turbines. These studies of idealized field sites have produced useful data for investigating the effects of simple terrain obstructions on average atmospheric flow and identifying specific deficiencies in numerical flow solutions; however, such sites are not representative of the wide range of regions where terrain-induced winds occur. As a result, these data do not provide sufficient test data for evaluating spatial representation of modeled flows for commonly occurring types of terrain features, such as isolated terrain obstacles with complex geometries, dissected montane environments, and steep river canyons. Other types of observational studies, such as those designed to investigate boundary layer evolution or convection-driven processes, have focused on characterizing the vertical distribution of wind, temperature, and moisture, but do not typically characterize the spatial variability in the near-surface wind field. Examples of the types of flow phenomenon that are of interest for high resolution model evaluations include 1) local surface layer flow decoupling from larger-scale atmospheric flow, 2) diurnal slope flows; 3) mountain-valley flows; 4) mountain-plain flows; and 4) the interactions of these effects at multiple spatial and temporal scales.

This study consisted of a field campaign focused on the collection of high resolution wind data from two different types of terrain features. Here we provide an overview of the data, with particular emphasis on the spatial characteristics of the surface wind measurements, and describe some unique flow features at each site.

The following presents: 1) a description of two study sites exhibiting different types of complex terrain features; 2) methods followed to collect detailed high resolution wind data over a range of meteorological conditions at each site; 3) an overview of the local meteorology and predominant flow field at each site; 4) unique surface flow features measured at each site; and 5) a description of how to access to the datasets. The data collected during this field campaign are used in a companion paper (Wagenbrenner et al., in Preparation) to evaluate several different NWP models and downscaling methods.

2 Site Descriptions

2.1 Big Southern Butte (BSB)

BSB is a volcanic dome cinder cone approximately 4 km wide that rises 800 m above the Upper Snake River Plain (USRP) in southeastern Idaho (43.3959, -113.0225) (Fig. 1). The dominant vegetation on the USRP and BSB is grass and sagebrush (generally < 1 m tall), although a few north-facing slopes on the butte have some isolated stands of 3-10 m tall timber. Average slopes range from 30 to 40% with nearly vertical cliffs in some locations. The USRP is essentially flat terrain surrounding BSB and extends more than 120 km to the north, east, south, and southwest (Fig. 2). The USRP is bordered by tall mountain ranges to the northwest and southeast. There are three prominent drainages (Big Lost River, Little Lost River, and Birch Creek) that flow southeast onto the USRP to the north of BSB (Fig.

136 2). These mountain-valley features contribute to thermally-driven diurnal flows and
137 formation of convergence zones on the USRP. Nighttime down-valley flows on the
138 USRP are from the northeast and daytime up-drainage flows are from the southwest.

139   Typical summertime winds on the Snake River Plain are primarily thermally driven
140 with strong upvalley winds during the day and relatively weaker downvalley winds at
141 night. The regional nocturnal northeasterly drainage flows usually subside by late
142 morning, and winds begin to rotate clockwise to southwesterly flow, then speeds
143 increase sharply by mid-to-late afternoon. The strongest southwesterly wind events
144 in the summer are associated with the passage of frontal systems.

145   Additionally, this region experiences occasional passage of very strong frontal
146 systems which bring westerly winds that become channeled into southwesterly flow
147 up the Lower Snake River Plain (LSRP) toward BSB (e.g, Andretta, 2002). This
148 same westerly synoptic flow passes over the mountains to the north of BSB and
149 surface winds become channeled into northerly flow down the Big Lost, Little Lost,
150 and Birch Creek drainages and onto the USRP. This northerly flow approaches BSB
151 from the USRP, eventually converging with the southwesterly flow somewhere in the
152 vicinity of BSB in what is referred to as the Snake River Plain Convergent Zone
153 (SPCZ) (Andretta, 2002; Andretta and Hazen, 1998). When an SPCZ forms, its
154 location shifts up or down the SRP depending on the strength of the low-level winds
155 over the USRP versus the LSRP (Andretta, 2002). SPCZ events most commonly
156 occur during the winter and spring, but occasionally form during other time periods as
157 well. Although formation of the SPCZ is not a frequent phenomenon during summer
158 conditions, we did observe a few flow events that may have been associated with the
159 SPCZ during our field campaign. Because the strong frontal systems which lead to
160 formation of the SPCZ result in complicated near-surface flows on and around BSB,
161 we investigate the observed flow events possibly associated with SPCZ-like
162 conditions in detail in Section 5.1.2.

163 **2.2 Salmon River Canyon (SRC)**

164 The field site was a 5 km long stretch of river located approximately 20 km east
165 (upstream) of Riggins, ID (45.4016, -116.2266) (Fig. 3) and spanning in elevation
166 from the canyon bottom (550 m) to the ridgetops (1600 m). The river canyon follows
167 a nearly straight east-west path within this extent. Prevailing winds in this region are
168 from the west. The predominant vegetation is grass (generally < 0.5 m tall), with
169 some timber in the higher elevations on the north aspects. Our instrumentation was
170 deployed away from forested areas, so as to avoid effects of the forest canopy on the
171 wind flow. There were prominent side drainages entering SRC on the east and west
172 end of our study area (Fig. 3).

173 **3 Instrumentation**

174 Each field site was instrumented with a network of surface wind sensors deployed
175 over a several month period (hereafter referred to as the monitoring period) and
176 supplemented with short term deployment of sonic anemometers and ground-based
177 vertical profiling instruments. Spatially dense arrays of more than 50 cup-and-vane
178 anemometers (S-WCA-M003, Onset Computer Corporation) measured wind speeds
179 and directions at 3.3 m above ground level (AGL) to characterize surface flow
180 patterns over and within the terrain features. Wind speed and direction data were
181 measured at 1 Hz and 30-second average wind speeds, peak gusts, and average

182 directions were recorded. The cup and vane has a measurement range of 0 to 44 m
183 s^{-1}, accuracy of +- 0.5 m s^{-1} and +- 5 degrees with resolution of 0.19 m s^{-1} and 1.4
184 degrees. These surface measurements were complemented by sonic anemometers
185 (CSAT3, Campbell Scientific, Inc.; SATI/3Vx, Applied Technologies, Inc.) and vertical
186 profiling instruments (MFAS, Scintech) at select locations and times (Table 1; Fig. 1
187 and 3) in order to provide measures of turbulence, friction velocity, and sensible heat
188 flux in near surface flows as well as to characterize flows aloft. The Campbell
189 Scientific CSAT3 sonic anemometers have a measurement rate of 1 to 60 hz, with
190 resolution of 1 mm s^{-1}, 0.5 mm s^{-1} and 15 mm s^{-1} for ux and uy, uz, and c
191 respectively, with a direction resolution of 0.06 degrees rms. The SATI/3Vx has
192 measurement range of 0 to 20 m s^{-1}, with resolution of 10 mm s^{-1} and 0.1 degrees.
193 The Scintech MFAS samples velocities from 0 to 50 m s^{-1} up to 1000 m agl over 1 to
194 60 min averaging intervals, with horizontal wind speed uncertainty of 0.3 m s^{-1} and
195 vertical wind speed accuracy of 0.1 m s^{-1} and directional uncertainty less than 1.5
196 degrees. Radiosonde (iMet-1, International Met Systems) launches were conducted
197 to characterize large-scale flows aloft for select time periods at each site. The Imet-1
198 system has a maximum range of 250 km to an altitude of 30 km and measures air
199 pressure, temperature, and humidity. Wind speed is calculated from onboard GPS
200 measurements. Accuracy is 0.5 hPa in pressure, 0.2°C in temperature, and 5 % in
201 RH. Wind speed is accurate to within 1 m s^{-1} and is updated at 1 Hz. Altitude is
202 accurate to within 15 m. Weather stations (WXT520, Vaisala) measured relative
203 humidity, air temperature, wind speed and direction, solar radiation, and precipitation
204 2 m AGL at two locations (Table 2; Fig 1 and 3). The Vaisala WXT520 measures air
205 temperature to 60C with +-0.3°C accuracy and 0.1C resolution, Wind speed is
206 measured from 0 to 60 m s^{-1} with 0.25 s response time and +-3% accuracy in speed
207 and 0.1 degree accuracy in direction.

208   The sampling layouts were designed to obtain measures of the upwind approach
209 flows as well as perturbations to the approach flow associated with the terrain
210 features. For each site, the extent of the sensor array covered an area that spanned
211 one to several mesoscale weather forecast grids of typical routine forecast resolution
212 (4 to 12 km) and the spatial density of the surface sensors was fine enough to
213 resolve flow patterns at the sub-grid scale (Fig. 1). Two field sites were selected to
214 represent an isolated terrain obstacle and a steep, non-forested river canyon. These
215 sites provided a range of wind conditions representative of generally dry, inland,
216 montane locations during summertime periods.

217   An array of 53 surface sensors was deployed on BSB between 15 June 2010 to 9
218 September 2010 (Fig. 1). Sensors were deployed along two transects running
219 southwest to northeast. A number of randomly located sensors were added along
220 and outside the two transects to increase the spatial coverage on and around the
221 BSB. A sodar profiler was deployed 2 km southwest of the butte from 1 July to 18
222 July, 2010 and immediately northeast of the butte from 31 August to 1 September,
223 2010 (Fig. 1; Table 1). A tower of sonic anemometers was deployed 2 km southwest
224 of the butte from 14 July to 18 July, 2010 (Fig. 1; Table 1). Three Radiosonde
225 launches were conducted at BSB from 31 August to 2 September, 2010 (Table 2).

226   An array of 27 surface sensors was deployed in three cross-river transects at
227 SRC from 14 July to 13 September, 2011 (Fig 3). Sodars and sonic anemometers
228 were operated from 16 July to 18 July and 29 August to 31 August, 2011 (Table 1).
229 Sodars were located in the valley bottom on the north side of the river and at the

230 ridgetop on the north side of the river near the east end of the field site (Fig. 3).
231 Sonics were operated on north and south ridgetops near the west end of the study
232 area and at two locations in the valley bottom on the north side of the river (Fig. 1).
233 Two weather stations monitored air temperature, relative humidity, precipitation, solar
234 radiation, wind speed, and wind direction; one was located on the southern ridgetop
235 at the east end of the field site and the other was located in the valley bottom on the
236 north side of the river (Fig. 3). Six RadioSonde launches were conducted on 18
237 August, 2011 (Table 2).

238   Additionally, the National Oceanic and Atmospheric Administration Field
239 Research Division (NOAA-FRD) operates a permanent mesonet system that consists
240 of 35 towers spread across the Idaho National Laboratory (INL) located on the USRP
241 and encompassing the BSB study area
242 (http://www.noaa.inel.gov/capabilities/mesonet/mesonet.htm;http://niwc.noaa.inel.gov
243 /). The mesonet towers measure wind speed, wind direction, air temperature,
244 relative humidity, and solar radiation. NOAA-FRD operates a permanent wind
245 profiling system (915 MHz radar profiler) and radio acoustic sounding system (RASS)
246 at a location approximately 10 km northeast of BSB. NOAA-FRD also operated a
247 mobile Radian Model 600PA SoDAR approximately 5 km south of BSB and an
248 Atmospheric Systems Corp. (ASC) Model 4000 mini SoDAR 15 km south of BSB 15
249 July to 18 July, 2010 and 31 August to 2 September, 2010.

250

251 **4   Analysis Methods and Terminology**

252 The data analyses presented here focus on the surface wind measurements and
253 terrain influences on the surface flow characteristics determined from these
254 measurements. All data are available in public archives as described in section 5.3.
255 All times presented are local daylight time to provide perspective on diurnal flow
256 regimes.

257 **4.1   Partitioning surface data into flow regimes**

258 The surface wind data are partitioned into four distinct wind regimes in order to
259 facilitate the analysis of typical diurnal flows in the absence of strong synoptic forcing
260 and high wind events during periods of strong synoptic forcing. The four wind
261 regimes are:

262   (1) A downslope regime, which included downslope and downvalley flows, forced
263 by nighttime surface cooling under weak synoptic forcing.

264   (2) An upslope regime, which included upslope and upvalley flows, forced by
265 daytime surface heating under weak synoptic forcing.

266   (3) An afternoon regime, during which local flows were influenced by larger scale
267 flows, either through convective mixing (at BSB) or through formation of upvalley
268 drainage winds (at SRC) under weak synoptic forcing.

269   (4) A synoptically forced regime, during which the normal diurnal cycle was
270 disrupted by strong larger scale flows typically correlated with gradient level winds
271 due to mechanically-induced turbulent mixing in the boundary layer.

272   The first three are analogous to the wind regimes described in Banta and Cotton
273 (1982) and are referred to collectively in this paper as the diurnal wind regime. The

274 diurnal wind regime persisted during periods of weak synoptic forcing. The fourth
275 regime was included here as the field sites investigated in this study frequently
276 experienced periods of intense large-scale synoptic forcing which generated high
277 surface wind speeds and sufficient mechanical mixing to overcome the diurnal flow
278 regime.

279 The following procedure was used to partition the surface data into these flow
280 regimes. First, periods during which the wind speed exceeded a threshold wind
281 speed at a surface sensor chosen to be representative of the large-scale flow at each
282 site were partitioned into a fourth, synoptically forced, regime (4). Threshold wind
283 speeds were selected for each site based on visual inspection of the wind speed time
284 series data for the chosen sensors. Thresholds were selected to be speeds that
285 were slightly above the typical daily peak speed for the chosen sensors. In other
286 words, the threshold speed was only exceeded when synoptic forcing disrupted the
287 typical diurnal wind regime at a given site. Speeds below the threshold are indicative
288 of periods of weak synoptic forcing, during which the diurnal wind regime prevails.
289 Sensors R2 and NM1 were chosen to be the representative sensors at BSB and
290 SRC, respectively. R2 was located on the USRP approximately 5 km southwest of
291 the butte at 1570 m elevation. NM1 was located on the north side of the SRC at
292 1530 m ASL, roughly three-quarters of the distance from the canyon bottom to the
293 ridgetop. These sensors were chosen because they appeared to be the least
294 influenced by the terrain and most representative of the gradient level winds.
295 Threshold velocities of 6 and 5 m s^{-1} were chosen for BSB and SRC, respectively
296 (Fig 4). 83% and 80% of the data fell below these threshold speeds at BSB and
297 SRC, respectively. Speeds below these thresholds fall within the range of diurnal
298 wind flows reported in the literature (Horst and Doran, 1986) and visual inspection of
299 the vector maps further confirmed this choice of threshold wind speeds, as all four
300 regimes were clearly identified by the surface flow patterns at each site.

301 After filtering out the synoptically driven periods, the remaining data were then
302 partitioned into regimes (1) to (3) based on visual inspection of the hourly vector
303 maps. Periods which exhibited clearly defined downslope flow were partitioned into
304 regime (1). Periods which exhibited clearly defined upslope flow were partitioned into
305 regime (2). And afternoon periods during which the upslope regime was disturbed
306 were partitioned into regime (3). Transition periods from one regime to another were
307 also identified based on visual inspection of the hourly vector maps.

308 The NOAA-FRD mesonet sensor at the summit of BSB (Fig. 1a, SUM) as well as
309 archived North American Mesoscale Model (NAM) forecasts were reviewed for
310 indications of upper-level flows that may have been decoupled from surface
311 measurements. References in the text to upper-level or gradient-level winds refer to
312 flows from these data sources.

313 **4.2 Data Averaging**

314 Surface wind observations were averaged over a 10-min period at the top of each
315 hour to represent an average speed valid at the top of each hour. This averaging
316 scheme was chosen to be representative of wind speeds from NWP forecasts.
317 Although NWP output is valid at a particular instant in time, there is some inherent
318 averaging in these 'instantaneous' predictions. The averaging associated with a
319 given prediction depends on the time-step and grid spacing used in the NWP model,

320 but is typically on the order of minutes. The 10-min averages are referred to in the
321 text as 'hourly' data.

322   Hourly vector maps were used to visualize the spatial patterns of the wind fields
323 for classifying flow regimes. The vector maps were produced by partitioning the
324 hourly data into one of two categories: (1) strong synoptic forcing or (2) weak
325 synoptic forcing (i.e., diurnal winds dominate), and then averaging the hourly data
326 (for each sensor) within each category over the entire monitoring period. The result
327 is an hourly average wind vector at each sensor location for each flow category. For
328 example, a vector map for 1300 hours under weak synoptic forcing would be
329 produced by filtering out the periods of strong synoptic forcing and then averaging all
330 hourly flow data for the 1300 hour at each sensor over the entire monitoring period.
331 Partitioning of data into weak vs. strong synoptic forcing was described in Section
332 4.1.

333   All data analysis and visualization was performed in R (R Core Team, 2013).
334 Vector maps were produced using the ggmap library (Kahle and Wickam, 2013) and
335 diurnal wind contour plots were produced using the metvurst library (Salabim, 2013).

336

5   Results and Discussion

338 Results for BSB are presented in section 5.1. Results for SRC are presented in
339 section 5.2. Average flows for the diurnal wind regimes are presented for each site
340 and then the disturbance to the diurnal wind regime by synoptic-scale forcing is
341 described. Transitions within the diurnal wind regime (e.g., upslope to afternoon
342 regime) occurred at roughly the same time of day throughout the monitoring periods,
343 with no discernible differences between average hourly vector maps for the first and
344 second half of the monitoring period. Thus, results for diurnal winds are reported as
345 averages for the entire monitoring period. This is reasonable since monitoring
346 periods were during summertime conditions at both sites.

347

5.1   BSB

5.1.1 Diurnal Winds: Upslope, Afternoon, and Downslope Regimes

350 Diurnal slope winds are driven by solar-induced horizontal temperature gradients be-
351 tween the ground surface and the air. Whiteman (2000) provides a thorough discus-
352 sion of diurnal mountain winds. The diurnal wind regime for an isolated mountain is
353 typically characterized by upslope winds during the day due to local solar heating of
354 the surface and downslope winds at night due to local surface cooling. An afternoon,
355 or coupled, regime often develops when gradient level winds become mixed in with
356 the growing surface layer. There is a transition phase between each phase of the
357 diurnal cycle as the temperature structure of the atmosphere responds and adjusts to
358 the changing incident solar radiation at the surface. The daily cycle can be disturbed
359 by interference from larger-scale winds.

360   Sunrise ranged from 0600 to 0700 during the monitoring period. Upslope winds
361 formed between 0800 and 0900 and the upslope regime was fully established by
362 1000 and persisted until around 1200. Upslope winds peaked around 1100. This

8

363 regime was characterized by thermally-driven upslope winds on all sides of the butte
364 flowing up from the surrounding SRP (Fig 5). The timing of onset and occurrence of
365 peak winds in the upslope regime was consistent with Banta and Cotton (1982) and
366 Geerts et al. (2008), who reported peaks in upslope flow before local solar noon
367 (LSN) for relatively small mountains. Others have reported later peaks in upslope
368 flow after LSN for larger mountain ranges (McNider and Pielke, 1981; Reiter and
369 Tang, 1984). Geerts et al. (2008) discussed this discrepancy in the reported timing
370 of upslope flows for different mountain ranges and described the development of
371 upslope winds as scaling with the size of the mountain. BSB is a relatively small iso-
372 lated mountain (by Geerts et al. (2008) terminology; horizontal scale of ~5 km and
373 vertical scale of ~800 m above the surrounding SRP), and so establishment of the
374 upslope regime prior to LSN fits with this scaling theory. Upslope flows persisted
375 about two hours longer than those at the South Park site in Colorado reported by
376 Banta and Cotton (1982). This difference could be attributed to the upwind terrain,
377 as westerly flows from the Rocky Mountains at the South Park Site were likely more
378 turbulent than the southwesterly flows approaching BSB from the SRP, and perhaps
379 were able to more quickly entrain the developing convective boundary layer (CBL) at
380 South Park.

381   Wind speeds in the upslope regime ranged from 1.8 to 7.3 m s^{-1}, with an average
382 of 3.1 m s^{-1} (Table 3). There were a few ridgetop sensors which appeared to be de-
383 coupled from the diurnal flow regime on the butte (discussed in detail at the end of
384 this section); if these sensors are removed, the wind speeds ranged from 1.8 to 4.5
385 m s^{-1}, with an average of 3.0 m s^{-1}. These are higher speeds than those reported by
386 Geerts et al. (2008), but similar to the range reported by Banta and Cotton (1982).
387 Differences in the reported range of speeds between this study and Geerts et al.
388 (2008) could be attributed to differences in the actual quantities reported. Geerts et
389 al. (2008) used an averaging scheme to calculate a mean anabatic wind that is a
390 function of the circumference of the polygon obtained by connecting the midpoints
391 between observation stations around the mountain. Also, their wind measurements
392 were made at 10 m AGL, while ours were made at 3.3 m AGL. Upslope wind speeds
393 were typically higher further up the slopes than lower on the butte (Fig. 6a; Fig 7).
394 Ridgetop sensors also appeared to be less coupled with the diurnal flow regime on
395 the butte and more correlated with the large-scale flows; this is confirmed by contour
396 plots of wind direction over time (Fig. 7) and is discussed in further detail at the end
397 of this section.

398   Upslope winds transitioned to the afternoon regime between 1200 and 1300.
399 This transition is most notable by an increase in wind speeds on the southwest side
400 of the butte and a shift in the wind directions on the northeast side of the butte (Fig.
401 5). This regime included local flows that generally correlated with the gradient level
402 winds above the ridgetops due to convective mixing in the deep afternoon boundary
403 layer. Convective mixing was fully established by 1400 hours and persisted until
404 around 2000 hours. Wind speeds peaked around 1500 hours and were fairly con-
405 sistent through 1900 hours. The onset of the afternoon regime was slightly later in
406 the day than that reported by Banta and Cotton (1982) which could be due to less
407 turbulent approach flow at BSB as discussed above. During the afternoon regime,
408 the prevailing southwesterly flow was routed around the northwest and southeast
409 sides of the butte (e.g., sensors R9 and R13). Wind speeds were highest on the
410 ridgetops and southwest slopes and lowest on the northeast slopes (Fig. 5). There

411 was some apparent recirculation on the northeast side of the butte as well as in some
412 of the side drainages (Fig. 5). Wind speeds in the afternoon regime ranged from 2.3
413 m s^{-1} to 8.1 m s^{-1} with an average of 4.1 m s^{-1}.

414   Sunset ranged from 2030 to 2130 hours during the monitoring period. The after-
415 noon regime began to decay and transition into downslope winds between 2100 and
416 2200 hours. The downslope regime was fully established by 2300 and persisted until
417 around 0800 hours. Peak downslope winds occurred around 0000 hours. The timing
418 of onset and occurrence of peak winds in the downslope regime agreed with obser-
419 vations reported in Banta and Cotton (1982). Downslope flows are clearly shown in
420 the hourly vector plots, with flows going from the top of the butte down all side drain-
421 ages around the butte and flowing out onto the SRP (Fig. 5). Wind speeds in the
422 downslope regime ranged from 1.3 to 12.0 m s^{-1}, with an average of 3.7 m s^{-1}. If the
423 decoupled ridgetop sensors are removed, the range was 1.3 to 7.5 m s^{-1}, with an av-
424 erage of 3.4 m s^{-1} (Table 3). This range is similar to that reported in Banta and Cot-
425 ton (1982) and slightly larger than that reported in Horst and Doran (1986). Others
426 have proposed an acceleration of flow with downslope distance due to thickening of
427 the katabatic layer from entrainment of ambient air into the slope flow and increased
428 buoyancy deficit with downslope distance (Horst and Doran, 1986); however, we did
429 not observe a consistent trend in wind speed with location on the slope (low vs. high)
430 during the downslope regime (Fig. 6b).

431   Diurnal winds dominated the local flows on and around the butte under periods of
432 weak synoptic forcing. During these periods, flow on and around BSB was decou-
433 pled from the large-scale atmospheric flows, except for high elevation ridgetop sen-
434 sors (R26, R35, TSW7) and one exposed mid- elevation ridge sensor (R15). This
435 decoupling is evident from the vector maps (Fig. 5) and is also confirmed by the con-
436 tour plots which show that these ridgetop locations do not experience the strong di-
437 urnal shifts in wind direction that other locations on and around the butte experience
438 (Fig. 7, 8). This ridgetop decoupling likely occurred because these locations were
439 high enough in the atmosphere to protrude out of the nocturnal boundary layer (NBL)
440 and the morning-time developing shallow CBL. Thus, the ridgetop winds were cou-
441 pled with the large-scale flows during all periods of the day. During nighttime hours
442 the ridgetop locations would experience residual layer winds and would only be cou-
443 pled with the rest of the flow on and around the butte once the residual layer was en-
444 trained by the growing shallow CBL and the convective mixing regime was fully es-
445 tablished. This proposed structure is confirmed by the vector plots, which show that
446 ridgetop winds did not change much from one regime to the next and only correlated
447 with winds at other nearby locations on the butte during the convective mixing regime
448 (Fig. 5).

449 5.1.2 Synoptic Disturbance of Diurnal Winds

450 Under periods of strong synoptic forcing, such as the passage of a cold front, the di-
451 urnal wind regime was disrupted and a synoptically-forced regime persisted. Two
452 types of flow events occurred within the synoptically-forced regime, one with south-
453 westerly flow and one with northeasterly flow (Fig. 9). The diurnal slope flows on
454 BSB were completely overtaken by the larger scale flows in this regime (Fig 9 vs. Fig.
455 5). During these events, daytime winds were consistently from the southwest, but in
456 a few cases, during nighttime and early morning hours, winds were from the north-
457 east (Fig. 9).

458   The southwest flows are referred to as 'synoptically driven upvalley' flows and the
459   northeasterly flows are referred to as 'synoptically driven downvalley' flows. Synopti-
460   cally driven upvalley flows were generally associated with the passage of cold fronts
461   from the west/southwest. Evolution of the synoptically driven downvalley flows is
462   more complex and some potential mechanisms are described below. Wind speeds
463   during the synoptically driven upvalley flows ranged from 2.9 to 20.3 m s^{-1}, with an
464   average of 7.1 m s^{-1}; the downvalley flow speeds ranged from 0.1 to 24.4 m s^{-1}, with
465   an average of 6.0 m s^{-1}. The synoptically driven downvalley (northeasterly) flows
466   occurred less frequently than the synoptically driven upvalley (southwesterly) flow
467   events; however, 4 distinct nighttime northeasterly flow events were observed during
468   the monitoring period.

469   There are at least three potential mechanisms which may have contributed to the
470   synoptically driven downvally events that we observed. One mechanism is related to
471   the SPCZ described in section 2.1. Mechanical channeling of the gradient level
472   winds by the surrounding terrain to the north and strong southwesterly flows on the
473   SRP can create an SPCZ-like convergence zone with strong upvalley winds to the
474   south of the zone and strong downvalley winds to the north of the zone. Winds at
475   BSB could be southwesterly or northeasterly depending on which side of the conver-
476   gence zone it was on. A second mechanism is based on observations from the NO-
477   AA-FRD mesonet suggesting that during summer months SPCZ-like events occur in
478   association with the passage of fronts or thunderstorm activity in the mountains to the
479   north. The former will often generate strong outflows through the northern valleys
480   onto the SRP, and the latter will sometimes generate outflow gust fronts. A third
481   possibility is that surface pressure gradients, in some cases, may have contributed to
482   the northeasterly flows. Two of the observed synoptically driven down valley flow
483   events occurred during periods where there was a strong northeast to southwest sur-
484   face pressure gradient which could have facilitated the flow; however, the other two
485   observed synoptically driven downvalley events did not occur during periods of fa-
486   vorable surface pressure gradients, so although surface pressure may be an influ-
487   ence, it was not the sole cause of these strong downvalley flow events. It is possible
488   that any of these three mechanisms may have contributed to the observed downval-
489   ley flows on BSB.

490   It is interesting that during periods of synoptically driven downvalley flows wind
491   speeds were generally higher on the southwest (leeward) side of BSB than on the
492   northeast (windward) side. Perhaps this is because the maximum in the synoptically
493   driven downvalley flow occurred at some higher elevation and was not well-mixed
494   with near-surface winds due to nighttime temperature stratification in the NBL. This
495   stratified flow could have become mixed into the surface flow at the ridgetops and
496   pulled down the southwest side of BSB. The northeasterly flow also would have
497   been enhanced by the nighttime downslope flow on the southwest side of BSB, thus
498   producing stronger winds on this side as compared to the northeast (windward side),
499   where the downslope flow would be in opposition (southwesterly) to the northeasterly
500   flow.

501

5.2 SRC

5.2.1 Diurnal Winds: Upslope, Afternoon, and Downslope Regimes

The diurnal wind regime for a canyon or valley is similar to that of the isolated mountain, with upslope/upvalley winds during the day due to local solar heating of the surface and downslope/downvalley winds at night due to local surface cooling. However, the afternoon, or coupled, regime often does not develop in deep or narrow canyons due to strong atmospheric decoupling of the canyon flows from the upper level winds (Banta and Cotton, 1982).

Sunrise ranged from 0500 to 0630 hours during the monitoring period at SRC. Upslope winds formed around 0900 hours and were fully established by 1000 hours, peaked around 1200 hours and persisted until around 1500 hours. The upslope regime was characterized by thermally-driven upslope winds on both sides of the canyon as well as up smaller side drainage slopes (Fig. 10). The one notable exception was sensor NM2, which experienced easterly or southeasterly flow during most periods of the day (Fig. 10). We believe this sensor was perhaps located in a local recirculation zone formed in the small side drainage; this is discussed at the end of this section. Wind speeds in the upslope regime ranged from 0.75 to 4.0 m s^{-1}, with an average of 2.4 m s^{-1} (Table 3).

Wind speeds tended to be highest at the upper elevation sensors around the onset of the upslope regime at 0900 hours (Fig. 11). As the upslope regime developed, wind speeds peaked around 1100 and were highest at the mid elevation sensors (Fig. 11) and this trend continued through 1300. The NW and SE transects do not follow these trends. The NW transect had consistently lower speeds at the mid elevation sensor during all periods of the upslope regime. This could be because NW3 was located slightly off of the ridge on a northwest aspect and perhaps decoupled from the flow along the rest of the NW transect. The SE transect had consistently higher speeds at the mid elevation sensor (SE4). The higher speeds at SE4 could be because this sensor was located on a ridge exposed to a prominent side drainage (Lake Creek) just to the east of our study area. Flows out of this Lake Creek drainage could have influenced this sensor more than others along the SE transect due to its location on the ridge and steep terrain to the southeast (Fig. 3).

We did not observe afternoon convective mixing at SRC as we did at BSB. This is consistent with Banta and Cotton (1982) who noted that a true convective mixing regime is not well documented in narrow mountain canyons, likely due to the strong channeling effect exerted by the canyon on the flow. The afternoon regime at SRC was characterized by a change from upslope to upvalley winds around 1500. This afternoon upvalley regime was fully established by 1600 and persisted through 1900. The most notable change between the upslope regime and the afternoon regime was the shift in wind direction from up the canyon walls (northerly or southerly flow) to upriver (westerly flow), especially for the lower elevation sensors. Daytime gradient level winds were typically from the west (upriver winds), so it could be difficult to determine if this afternoon shift in wind direction was driven by convective mixing of gradient level winds down into the canyon or the formation of thermally-driven upvalley flow within the canyon. The fact that this change in wind direction was most notable in the lower elevation sensors (Fig. 10) points to a thermally-driven mechanism. Wind speeds were fairly consistent throughout this time period and ranged from 0.92 to 4.2 m s^{-1}, with an average of 2.5 m s^{-1} (Table 3). Wind speeds were the lowest

near the canyon bottom except for the SE and NW transects, which had the lowest speeds at high and mid elevation sensors (SE3 and NW3). Both of these sensors were located slightly off of the main ridge. It is interesting that the lowest sensors responded most noticeably to the shift from upslope to upvalley flow with a change in wind direction, but that the highest speeds were still observed at the upper elevation sensors.

Sunset ranged from 1900 to 2030 hours during the monitoring period. Upvalley flow began to weaken and transition to downslope flow between 2000 and 2100. The downslope regime was fully established by 2200 and persisted until around 0700. Peak wind speeds in the downslope regime occurred around 2200. Wind speeds in the downslope flow regime ranged from 0.33 to 4.1 m s^{-1}, with an average of 1.2 m s^{-1} (Table 3). Wind speeds tended to increase with upslope distance (Fig. 12), with the exception of the SE transect, likely due to the location of SE3 and SE4 as discussed above. This trend was consistent throughout the duration of the downslope regime.

Diurnal trends were further inspected for the NM transect because it was not located near any prominent side drainages and likely exhibited the simplest flow characteristics. Contour plots show a strong diurnal signal for all sensors in this transect (Fig. 13), indicating that diurnal flows are a major flow feature in the SRC. Winds were from the east/southeast in the early morning and from the west/northwest in the afternoon and the highest speeds occurred at the upper elevation sensors during early morning hours. One exception was the NM2 sensor, which rarely experienced winds from the west/northwest and did not experience a morning time peak in wind speed. This sensor was located slightly off of a mid-slope ridge on a slope with a northwest aspect. We suspect that this location was possibly a zone of recirculation. The lowest sensor, NM4, also did not experience a morning peak in wind speed and rarely experienced winds from the northeast. The highest speeds occurred during periods of synoptic disturbance, which we believe had more of an effect at upper elevations in the SRC than lower ones near the river bottom. This is discussed further in the next section.

5.2.2 Synoptic Disturbance of Diurnal Winds

Two types of synoptic disturbances to the diurnal wind regime in the SRC were observed (Fig. 14). One is associated with the passage of frontal systems from the west, which brings strong westerly gradient winds. The other appears to be associated with the presence of an east-west pressure gradient that generates strong morning-time easterly flow. During the passage of frontal systems, westerly winds are channeled up the river canyon and most sensors in SRC (with the exception of those located in side drainages) experienced westerly flow. These events tended to occur during mid-afternoon hours. Wind speeds during this type of synoptic disturbance ranged from 2.1 to 5.7 m s^{-1}, with an average of 3.8 m s^{-1}.

The highest observed wind speeds in the SRC were from the east during morning hours (Fig. 13, 14). Wind speeds during these pressure-driven downvalley events ranged from 0.84 to 9.1 m s^{-1}, with an average of 3.1 m s^{-1}. These events occurred roughly every few days and appeared to be induced by a surface pressure gradient formed when a thermal trough existed on the Columbia Plateau to the northwest of SRC and high pressure existed to the east of SRC (Fig. 15). An east-west surface

13

pressure gradient existed on days when enhanced downvalley flow was observed. On days when the downvalley flow feature was not observed, there was no east-west surface pressure gradient. The highest wind speeds during this type of flow event were observed at the upper elevations of the SRC (Fig. 16). The east-west surface pressure gradient coupled with the typical nighttime/early morning katabatic flow in the canyon resulted in very strong downvalley winds in the SRC. This pressure-enhanced katabatic surface flow tended to be decoupled from the larger-scale gradient flow (which is typically from the west) during these pressure-driven events.

5.3 Archived Data

All data are archived as downloadable SQLite databases. Access to these databases along with tools to query, process, and visualize, the data is described at http://www.firemodels.org/index.php/windninja-introduction/windninja-publications. Descriptions of the NOAA mesonet data and contact information regarding mesonet data are found at http://www.noaa.inel.gov/capabilities/mesonet/mesonet.htm and http://niwc.noaa.inel.gov/ and http://niwc.noaa.inel.gov/.

6 Conclusions

We have presented an analysis of two high-resolution surface wind datasets, one collected from a tall isolated mountain, and the other from a steep river canyon. The wind data were analysed and presented in terms of four flow regimes: upslope, afternoon, downslope, and a synoptically-driven regime. These datasets constitute a unique inventory of surface wind measurements at very high spatial resolution under dry summertime conditions. Public access to the archived datasets has been described.

Surface winds on and around BSB were completely decoupled from large-scale flows during upslope and downslope flow regimes, except for the highest elevation ridgetop sensors. These ridgetop locations at BSB tended to correlate better with gradient-level winds than with the local diurnal surface flows. Surface winds in SRC were decoupled from large-scale flows except during periods of strong synoptic forcing that enhanced either upriver or downriver flows.

Wind speeds increased with distance upslope during the upslope regime at BSB, but generally decreased with distance upslope at SRC. Wind speed did not have a simple, consistent trend with position on the slope during the downslope regime at BSB, but generally increased with distance upslope at SRC. We did not observe a convective mixing regime at SRC under periods of weak synoptic forcing, only a transition from upslope to thermally-driven upriver flow.

The highest speeds measured at BSB occurred during the passage of frontal systems which generated strong southwesterly flows and during infrequent strong northwesterly flows presumably generated through SPCZ-like dynamics, thunderstorm outflows, or surface pressure gradients. Ridgetop winds were often twice as high as surface wind speeds measured on the surrounding SRP. The highest speeds measured at SRC occurred during late morning hours and were from easterly flows presumably produced by surface pressure gradients induced by formation of a thermal trough over the Columbia Plateau to the NW and high pressure to the east.

The highest wind speeds during these pressure-driven easterly flow events were measured at the mid to high elevation sensors.

These results have important implications for modeling near-surface winds in complex terrain. The fact that surface winds at both sites tended to be decoupled from large-scale flows under periods of weak synoptic forcing suggests that traditional operational weather model winds (i.e., with numerical grid resolutions of around 4 km or larger) are not likely to be good predictors of local winds in sub-grid scale complex terrain. Under periods of strong synoptic forcing, variability in surface winds was sufficiently large due to terrain-induced mechanical effects (speed-up over ridges and decreased speeds on leeward sides of terrain obstacles), that a mean wind for a 4 km grid cell encompassing these terrain features would not be representative of actual surface winds at most locations on or within the terrain feature. The findings from this work along with the additional archived data and available mesonet data at BSB should provide guidance for future development and evaluation of high-resolution wind models and integrated parameterizations, such as for simulating diurnal slope flows and non-neutral atmospheric stability effects.

References

667 **References**

668 Andretta, T.A., 2002. Climatology of the Snake River Plain convergence zone. Na-
669   tional Weather Digest. 26, 37–51.

670 Andretta, T.Z., Hazen, D.S., 1998. Doppler radar analysis of a Snake River Plain
671   convergence event. Weather and Forecasting. 13, 482–491.

672 Banta, R.M., 1984. Daytime boundary-layer evolution over mountainous terrain. Part
673   1: observations of the dry circulations. Mon. Wea. Rev. 112, 340–356.

674 Banta, R.M., Cotton, R., 1982. An analysis of the structure of local wind systems in a
675   broad mountain basin. J. Appl. Meteorol. 20, 1255–1266.

676 Beaucage, P., Brower, M.C., Tensen, J., 2012. Evaluation of four numerical wind flow
677   models for wind resource mapping. Wind Energy.

678 Berg, J., Mann, J., Bechmann, A., Courtney, M.S., Jørgensen, H.E., 2011. The Bo-
679   lund Experiment, Part I: Flow over a steep, three-dimensional hill. Boundary-
680   Layer Meteorol. 141, 219–243.

681 Chrust, M.F., Whiteman, C.D., Hoch, S.W., 2013. Observations of thermally driven
682   wind jets at the exit of Weber Canyon, Utah. J. Appl. Meteorol. Climatol. 52,
683   1187–1200.

684 Daly, C., Conklin, D.R., Unsworth, M.H., 2010. Local atmospheric decoupling in
685   complex topography alters climate change impacts. Int. J. Climatol. 30, 1857–
686   1864.

687 Defant, F. 1949. "Zur Theorie der Hangwinde, nebst Bermekungen sur Theorie der
688   Berg- und Talwinde." <u>Archiv fuer Meteorologie Geophysik und Bioklimatologie</u>
689   **Ser. A.**(1): 421-450.

690 Forthofer, J., Shannon, K., Butler, B., 2009. Simulating diurnally driven slope winds
691   with WindNinja. Eighth Symposium on Fire and Forest Meteorology. Oct 13-15.
692   Kalispell, MT.

693 Forthofer, J.M., Butler, B.W, Wagenbrenner, N.S., In Press. A comparison of two ap-
694   proaches for simulating fine-scale winds in support of wildland fire management:
695   Part 1 – model formulation and comparison against measurements. Int. J.
696   Wildland Fire.

697 Geerts, B., Miao, Q., Demko, J.C., 2008. Pressure perturbations and upslope flow
698   over a heated, isolated mountain. Mon. Wea. Rev. 136: 4272–4288.

699 Grell, G.A., Emeis, S., Stockwell, W.R., Schoenemeyer, T., Forkel, R., Michalakes,
700   J., Knoche, R., Seidl, W. 2000. Application of a multiscale, coupled
701   MM5/chemistry model to the complex terrain of the VOTALP valley campaign.
702   Atmos. Environ. 34, 1435–1453.

703 Horst, T.W., Doran, J.C., 1986. Nocturnal drainage flow on simple slopes. Boundary-
704   Layer Meteorol. 34: 263–286.

705 Jiménez, P., Jorba, O., Parra, R. Baldasano, J.M., 2006. Evaluation of MM5-
706   EMICAT2000-CMAQ performance and sensitivity in complex terrain: high-
707   resolution application to the northeastern Iberian peninsula. Atmos. Environ. 40,
708   5056–5072.

Jiménez, P., Dudhia, J., 2012. Improving the representation of resolved and unresolved topographic effects on surface wind in the WRF model. J. Appl. Meteorol. Climatol. 51, 300–316.

Kahle, D., Wickham, H., 2013. ggmap: A package for spatial visualization with Google Maps and OpenStreetMap. R package version 2.3. http://CRAN.R-project.org/package=ggmap.

Langhans, W., Juerg, S., Fuhrer, O., Bieri, S., Schär, C., 2013. Long-term simulations of thermally driven flows and orographic convection at convection-parameterizing and cloud-resolving resolutions. J. Appl. Meteor. Climatol. 52, 1490–1510.

Lundquist, K.A., Chow, F.K., Lundquist, J.K., 2010. An immersed boundary method for the Weather Research and Forecasting Model. Mon. Wea. Rev. 138:796–817.

McNider, R.T., Pielke, R.A., 1981. Dirunal boundary-layer development over sloping terrain. J. Atmos. Sci. 38: 2198–2212.

Palma, J.M.L.M., Castro, F.A., Ribeiro, L.F., Rodrigues, A.H., Pinto, A.P., 2008. Linear and nonlinear models in wind resource assessment and wind turbine micro-siting in complex terrain. J. Wind Engineer. Indust. Aerodynam. 96, 2308–2326.

R Core Team, 2013. R: A language and environment for statistical computing. R Foundation for Statistical Computing, Vienna, Austria. URL http://www.R-project.org/.

Reiter, E.R., Tang, M., 1984. Plateau effects on diurnal circulation patterns. Mon. Wea. Rev. 112: 638–651.

Rothermel, R.C., 1972. A mathematical model for predicting fire spread in wildland fuels: Ogden, UT, p. 40.

Salabim, T., 2013. Metvurst: meteorological visualization utilities using R for science and teaching. URL https://github.com/tim-salabim/metvurst.

Scire, J.S., Robe, F.R., Fernau, M.E., Yamartino, R.J., 2000. A user's guide for the CALMET meteorological model. Earth Tech, Inc.: Concord, MA.

Sharples, J.J., McRae, R.H.D., Wilkes, S.R., 2012. Wind-terrain effects on the propagation of wildfires in rugged terrain: fire channeling. Intern. J. Wild. Fire. 21, 282–296.

Simpson, C.C., Sharles, J.J., Evans, J.P., McCabe, M.F., 2013. Large eddy simulation of atypical wildland fire spread on leeward slopes. Intern. J. Wild. Fire. 22, 599–614.

Taylor, PA, Teunissen, HW 1987. The Askervein Hill Project: Overview and background data. Boundary-Layer Meteorology 39, 15-39.

Wagenbrenner, N.S., Lamb., B.K., Forthofer, J.M., Shannon, K.S., Butler, B.W., In preparation. Effect of model horizontal grid resolution on near-surface wind predictions in complex terrain: evaluations with high-resolution field observations from an isolated mountain and a steep river canyon. To be submitted to J. Appl. Meteorol. Climatol.

Whiteman, C.D. 2000. Mountain Meteorology: Fundamentals and Applications. Oxford University Press. New York.

752 Zardi, D, Whiteman, CD (2013) Diurnal Mountain Wind Systems. In 'Mountain
753   Weather Research and Forecasting.' (Eds FK Chow, SFJ De Wekker, BJ
754   Snyder.) pp. 35-119. Springer Netherlands. Chap 2

755 Zhong, S., Fast, J., 2003. An evaluation of MM5, RAMS, and Meso-Eta models at
756   subkilometer resolution using VTMX field campaign data in the Salt Lake valley.
757   Monthly Weather Review. 131, 1301–1322.
758

Table 1. Sonic anemometer and vertical profiling sensor details.

ID	Site[1]	Sensor	Model	Time Period	Averaging Period
WSU1	BSB	Sodar	Scintech	14 Jul–15 Jul 2010	30-min
		Sonic	ATI	14 Jul–18 Jul 2010	10 Hz
WSU2	BSB	Sodar	Scintech	15 Jul–19 Jul 2010	30-min
				31 Aug–1 Sep 2010	30-min
NOAA1	BSB	Sodar	Radian 600PA	14 Jul–19 Jul 2010	30-min
		Radar	Radian LAP-3000	14 Jul–19 Jul 2010	30-min
NOAA2	BSB	Sodar	ASC 4000	14 Jul–19 Jul 2010	30-min
ST1	SRC	Weather station	Viasala, WXT	16 Aug–12 Sep 2011	15-min
		Sonic	CSAT3	18 Aug–19 Aug 2011	10 Hz
ST2	SRC	Sodar	Scintech	16 Aug–18 Aug 2011	30-min
				29 Aug–31 Aug 2011	30-min
		Sonic	ATI	16 Aug–18 Aug 2011	10 Hz
ST3	SRC	Weather station	Viasala, WXT	17 Aug–12 Sep 2011	15-min
ST4	SRC	Sonic	ATI	16 Aug 19–Aug 2011	10 Hz

[1]BSB = Big Southern Butte; SRC = Salmon River Canyon.

19

762   Table 2. Radiosonde launches at BSB and SRC. Times are local.

Site[1]	Date	Time of launch
BSB	August 31 2010	16:57
	September 1 2010	16:59
	September 2 2010	10:35
SRC	July 18 2011	11:28
		13:56
		15:50
		18:14
		20:00
		21:32

763   [1] BSB = Big Southern Butte; SRC = Salmon River Canyon.

764

765 Table 3. Measured wind speeds (m s^{-1}) during upslope, downslope, and convective
766 mixing regimes at Big Southern Butte (BSB) and Salmon River Canyon (SRC).
767 Decoupled ridgetop locations (sensors R26, R35, TSW7, and R15) were omitted
768 from BSB averages; speeds in parentheses include ridgetop sensors.

Site	Wind Speed	Upslope (1100 LT)	Afternoon (1600 LT)	Downslope (0000 LT)
BSB[1]	Min (m s^{-1})	1.8	2.3	1.3
	Max (m s^{-1})	4.5 (7.3)	8.1	7.5 (12.0)
	Mean (m s^{-1})	3.0 (3.1)	4.1	3.4 (3.7)
SRC[1]	Min (m s^{-1})	0.75	0.92	0.33
	Max (m s^{-1})	4.0	4.2	4.1
	Mean (m s^{-1})	2.4	2.5	1.2

769 [1] BSB = Big Southern Butte; SRC = Salmon River Canyon
770
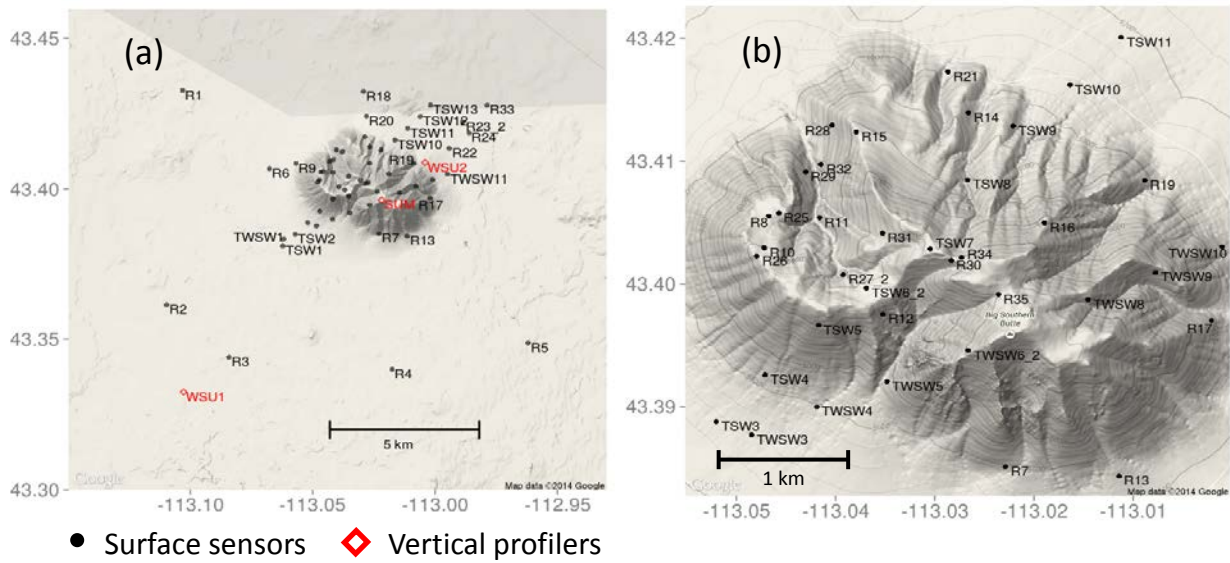
Fig. 1. Site overview and sensor layouts at the Big Southern Butte (a, b). Black circles indicate surface sensors. Red diamonds indicate sonic anemometers and vertical profiling sensors.

777

778
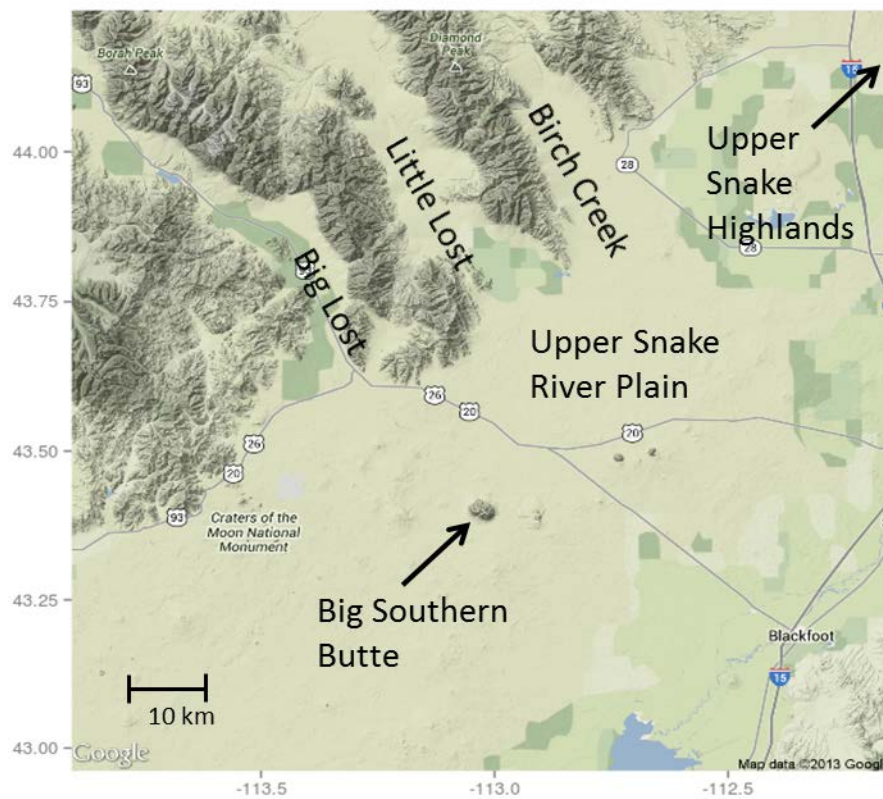
Fig. 2. Snake River Plain and prominent drainages surrounding the Big Southern
Butte study site. The topographical gradient is increasing in elevation from south to
north. Elevation of plain around Big Southern Butte is nominally 1585 m.

782
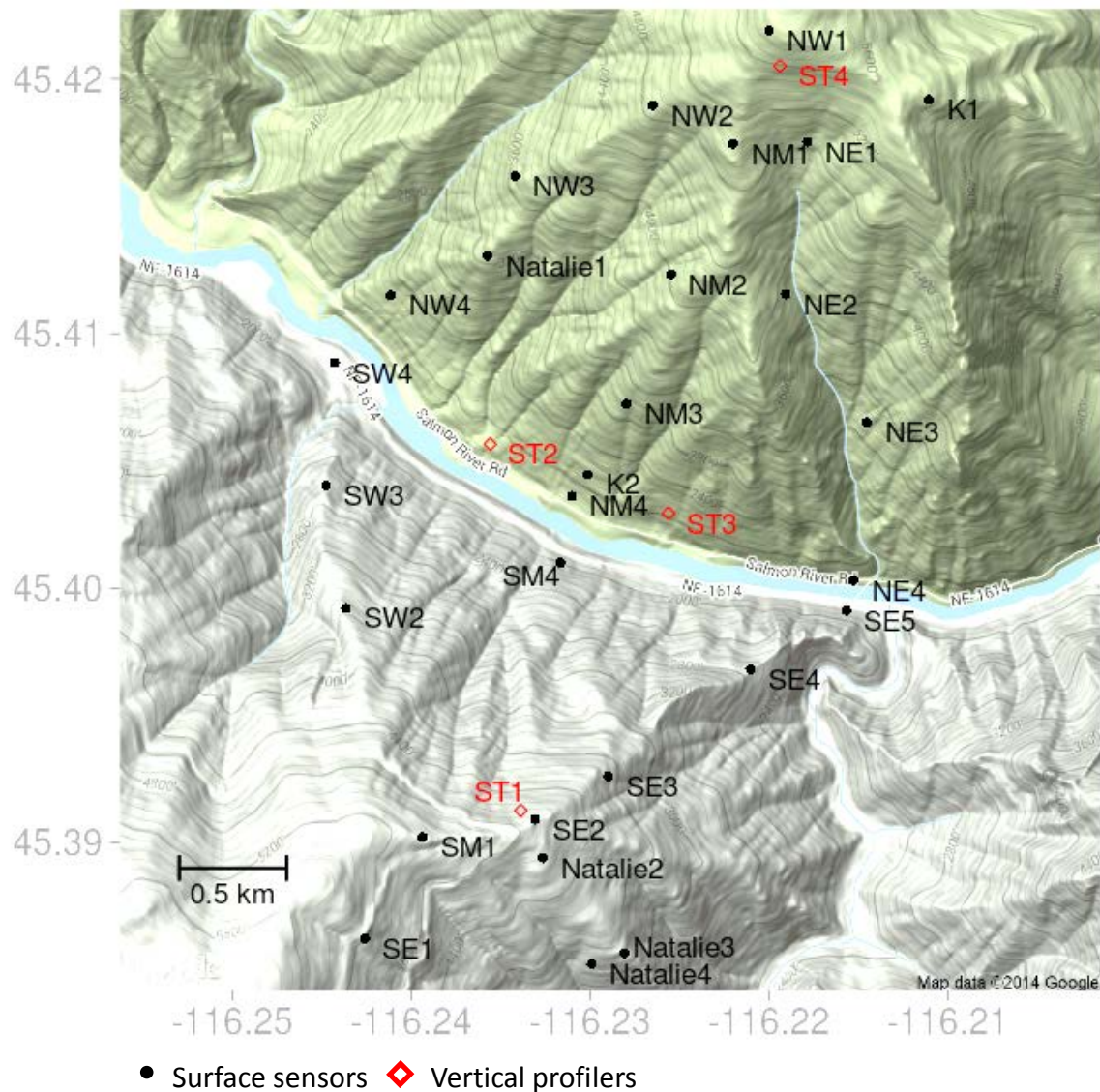
Fig. 3. Site overview and sensor layouts at the Salmon River Canyon. Black circles indicate surface sensors. Red diamonds indicate sonic anemometers and vertical profiling sensors. The topographical gradient is increasing in elevation from left to right. Elevation of river is 540 m.
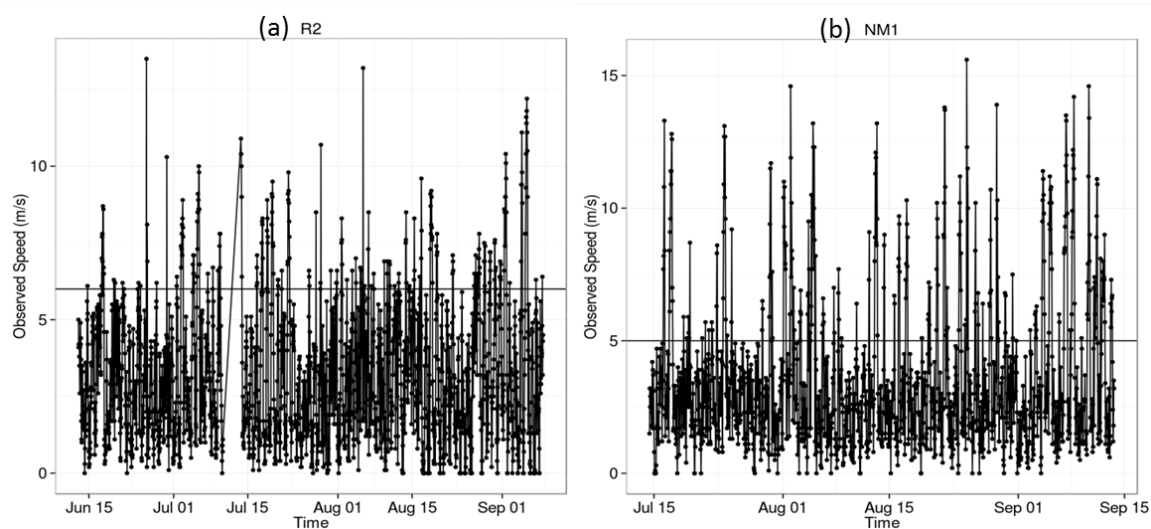
Fig. 4. Observed hourly wind speeds for sensor R2 at Big Southern Butte (elevation 1560 m) and NM1 (elevation 1734 m) at the Salmon River Canyon study site. The horizontal line indicates the threshold speed chosen to partition synoptically driven events from diurnal events.
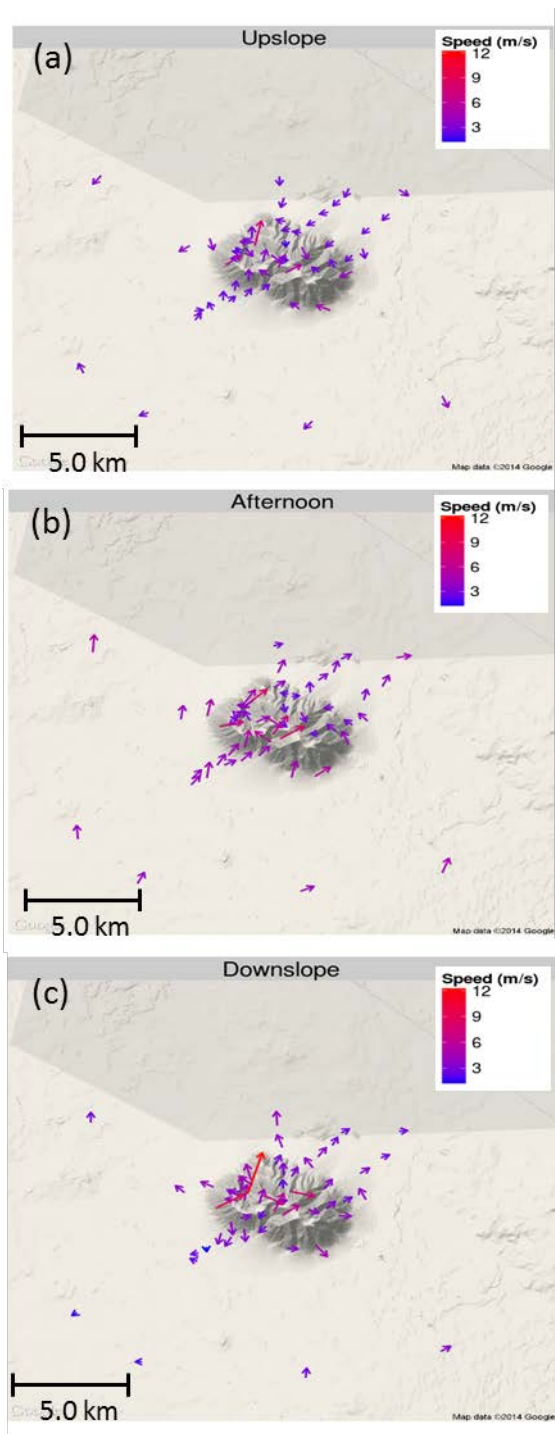
Fig. 5. Upslope (1100 local time) (a), afternoon (1600 local time) (b), and downslope (0000 local time) (c) flow regimes at Big Southern Butte during periods of weak synoptic flow between June-September 2010. Vectors are centered on sensor locations and represent the average hourly flow at a given sensor. Periods of strong synoptic forcing were removed prior to averaging.
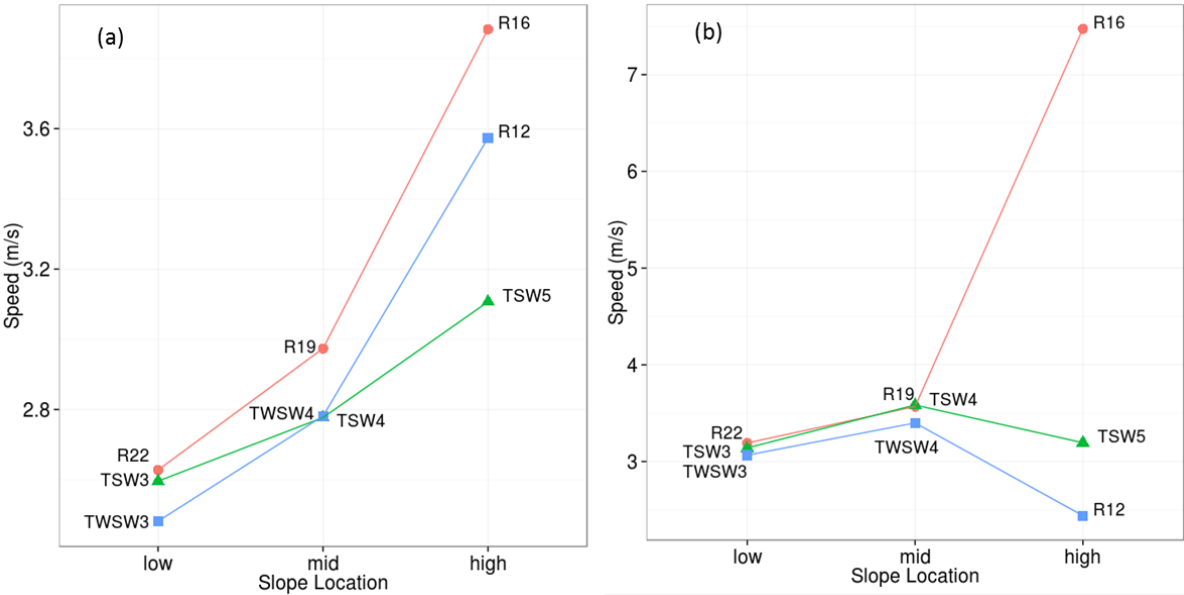
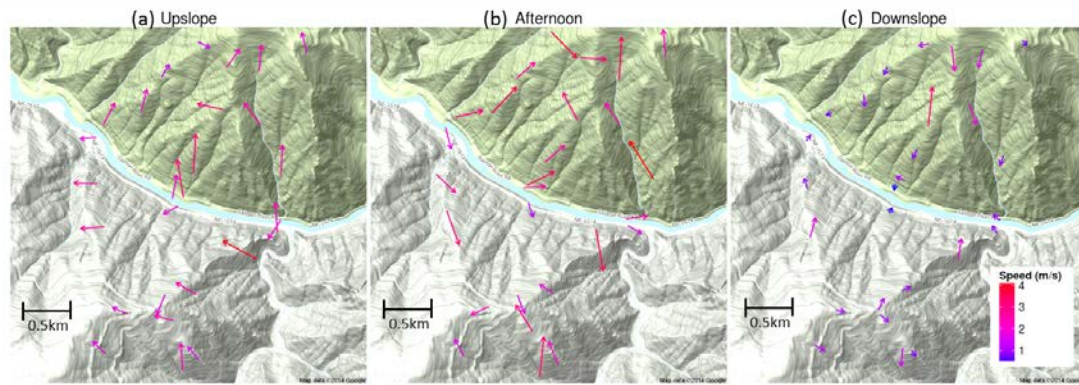805 Fig. 6. Average wind speeds for sensors at three slope locations (low, mid, and high)
806 along three transects during the (a) upslope (1100 local time) and (b) downslope
807 (0000 local time) flow regimes at Big Southern Butte.

808
809
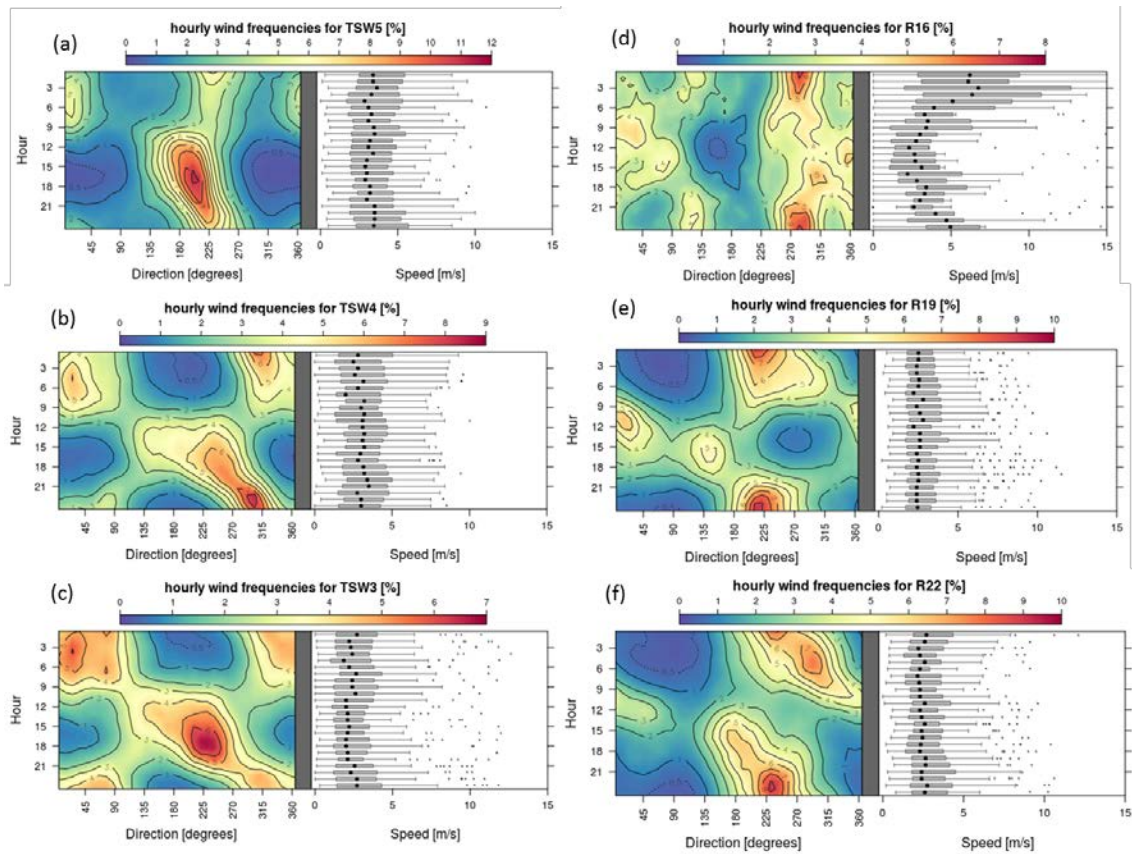
Fig.7. Contour plots of hourly wind frequencies and corresponding wind speeds for a transect on the southwest slope of Big Southern Butte (a)-TSW5 elevation 2067 m, (b)-TSW4 elevation 1750 m, (c)-TSW3 elevation 1630 m; and a transect on the northeast slope of Big Southern Butte (d)-R16 elevation 2080 m, (e)-R19 elevation 1720m, and (f)-R22 elevation 1550 m. Panels are ordered from higher elevation sensors (top panels) to lower elevation sensors (bottom panels). Periods of synoptic forcing were removed from this data.

819
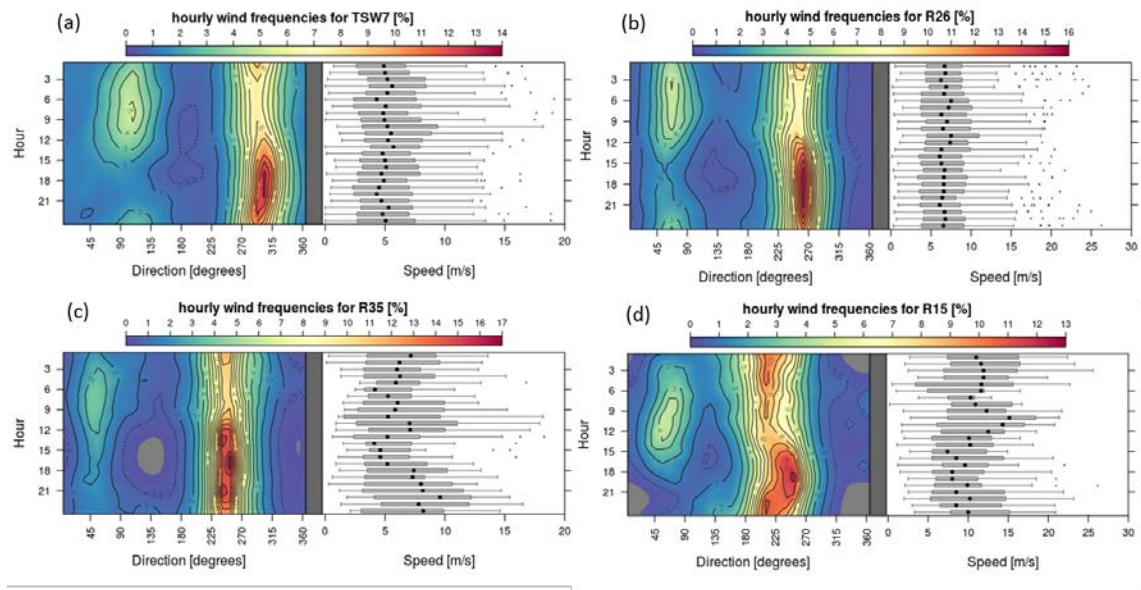
Fig. 8. Contour plots of hourly wind frequencies and corresponding wind speeds at four ridgetop locations at Big Southern Butte. (a)-TSW7 elevation 2217 m, (b)-R26 elevation 2100 m, (c)-R35 elevation 2200 m, (d)-R15 elevation 1980 m. Periods of strong synoptic forcing were removed from this data.
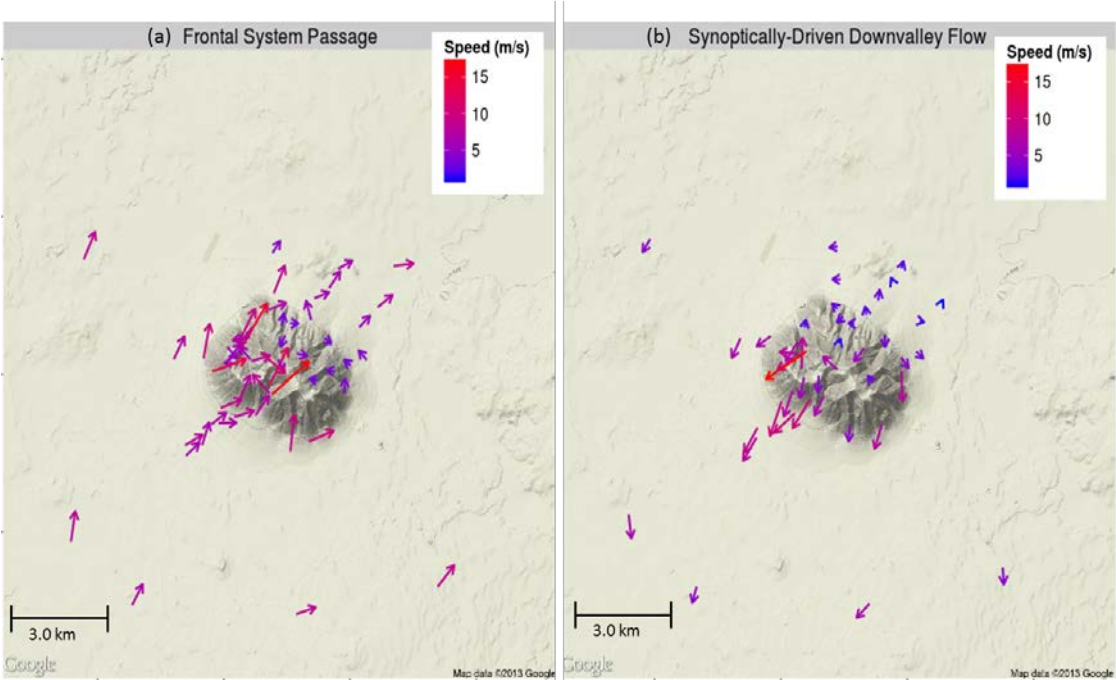
Fig. 9. Characteristic synoptically-driven regime events during the passage of a frontal system (1800 LT) (a) and during synoptically-enhanced downvalley flow on the Snake River Plain (2300 LT) (b) at Big Southern Butte during June-September 2010. Vectors represent the average hourly flow at a given sensor. Periods of weak synoptic forcing were removed prior to averaging.
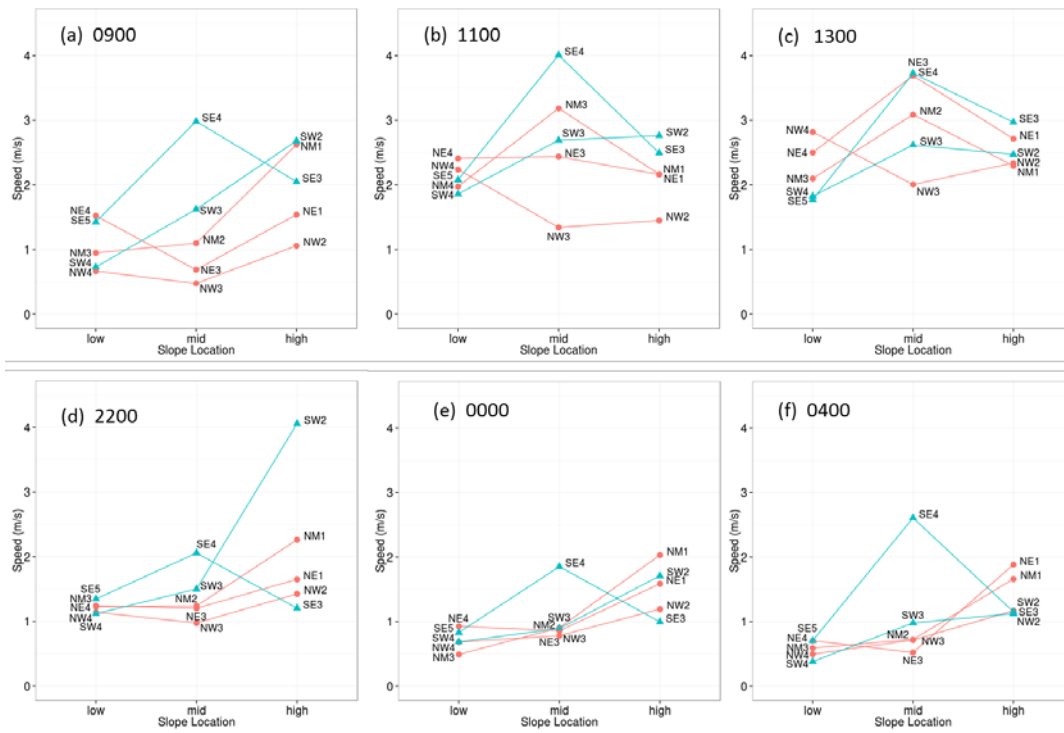
Fig. 10. Upslope (a) (1100 local time), afternoon (b) (1600 local time), and downslope (c) (0000 local time) regimes at the Salmon River Canyon site during periods of weak synoptic flow between July-September 2011. Vectors represent the average hourly flow at a given sensor. Periods of strong synoptic forcing were removed prior to averaging.
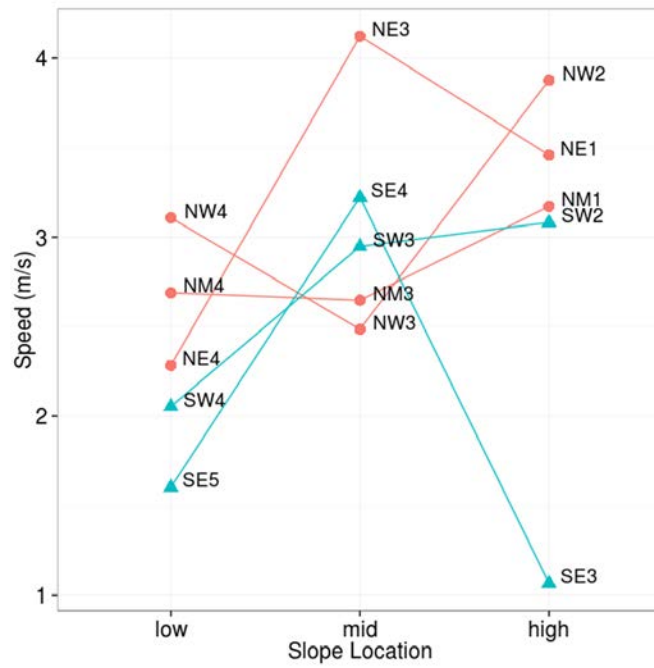
Fig. 11. Average wind speeds for sensors at three slope locations (low, mid, and high) along five transects during three hours of the upslope (a, b, c) and downslope (d, e, f) flow regimes at the Salmon River Canyon site. Blue and red lines are transects on the south and north side of the river, respectively.
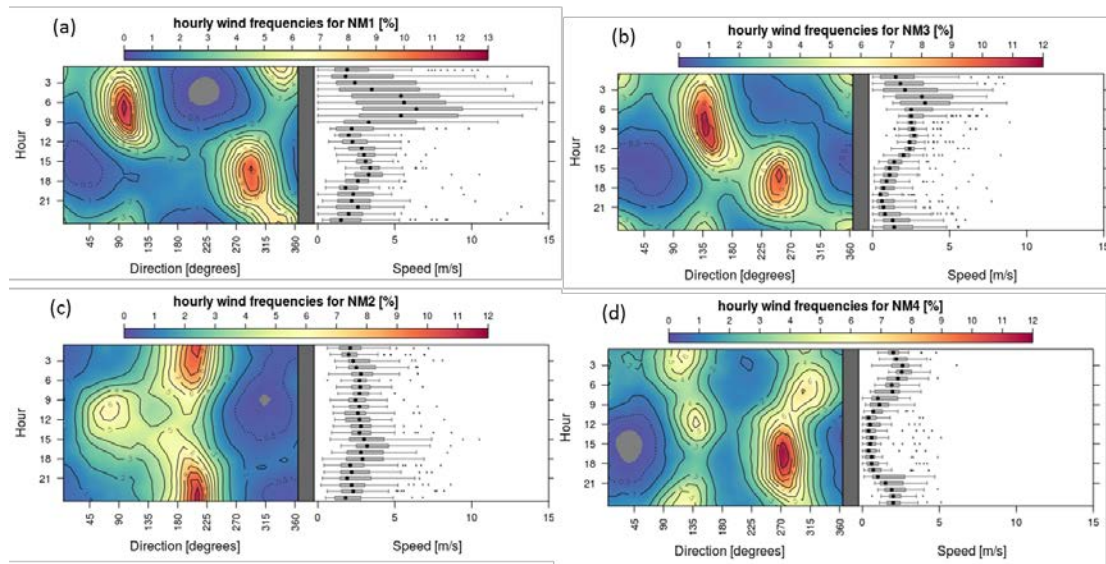
Fig. 12. Average wind speeds for sensors at three slope locations (low, mid, and high) along five transects during the afternoon flow regime (1700 local time) at the Salmon River Canyon site. Blue and red lines are transects on the south and north side of the river, respectively.

Fig. 13. Contour plots of hourly wind frequencies and corresponding wind speeds for the NM transect at the Salmon River Canyon site. (a)-NM1 is near the ridgetop at 1734 m. (b)-NM2 is at 1210 m. (c)-NM3 is at 1080 m. (d)-NM4 is at 540 m and is near the canyon bottom. All data were used.
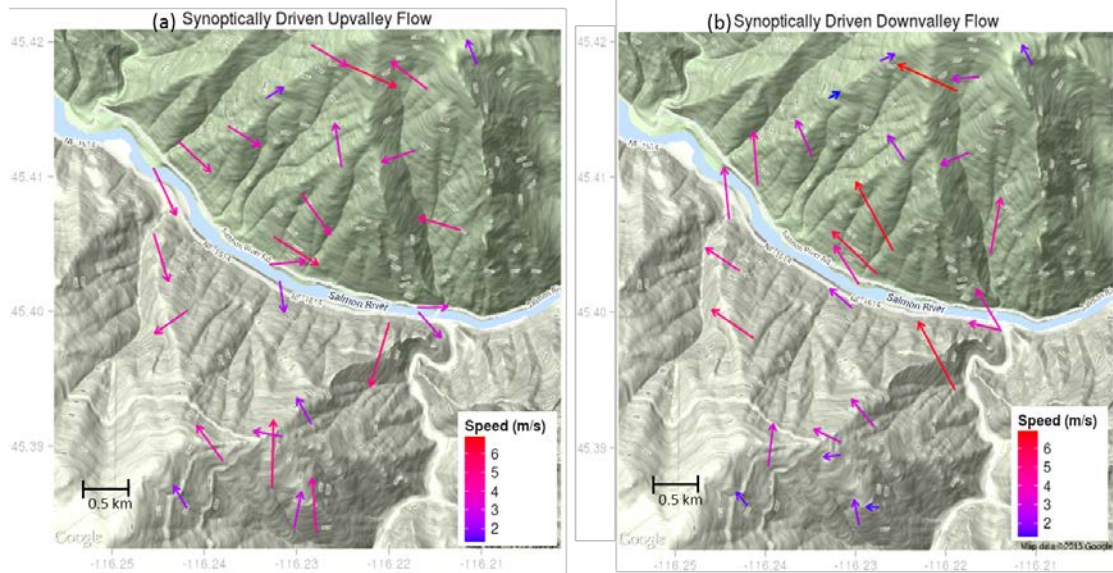
Fig. 14. Characteristic synoptically driven upvalley flow (1500 local time) (a) and downvalley flow (1100 local time) (b) at the Salmon River Canyon site during July-September 2011. Vectors represent the average hourly flow at a given sensor. Periods of weak synoptic forcing were removed prior to averaging.
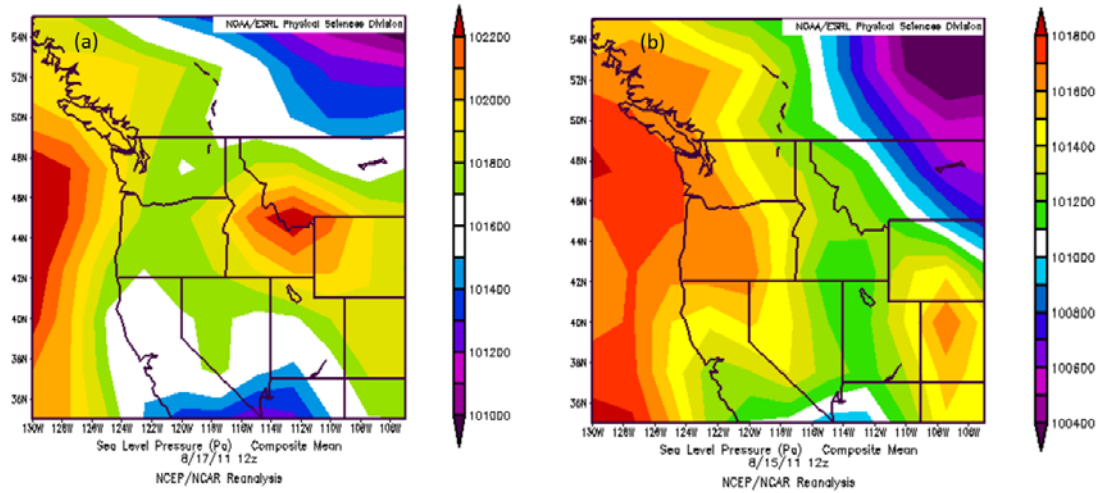
Fig. 15. Synoptic-scale surface pressure conditions conducive to enhanced easterly flow (a) and typical diurnal flow scenarios (b) at the Salmon River Canyon site (North American Regional Reanalysis data courtesy of National Center for Environmental Prediction).
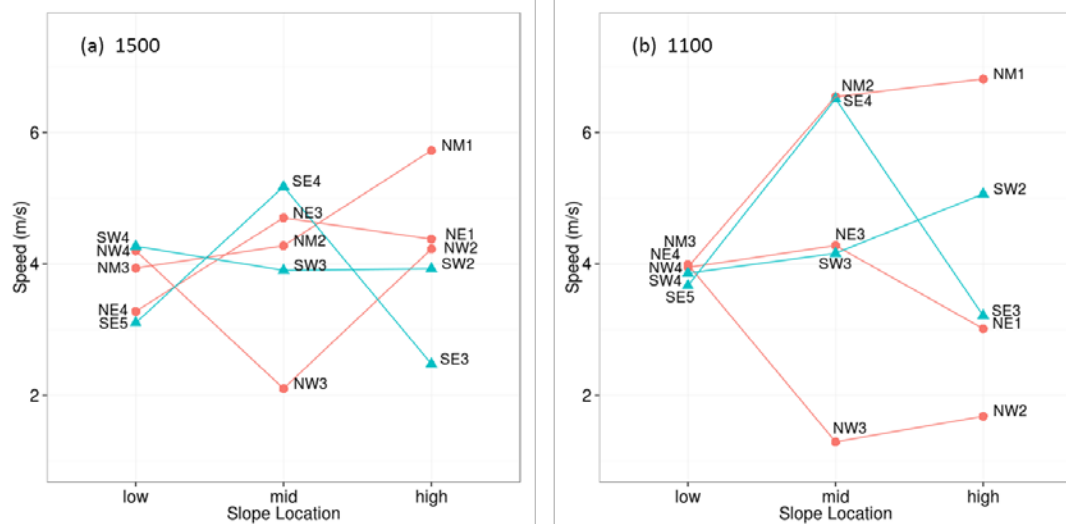
Fig. 16. Average wind speeds for sensors at three slope locations (low, mid, and high) along five transects during the synoptically driven upvalley (a) and synoptically driven downvalley (b) flow regimes at the Salmon River Canyon site. Blue and red lines are transects on the south and north side of the river, respectively.